

Vibrational response and temperature of shock-compressed Pt: *In situ* extended x-ray absorption fine structure measurements to 325 GPa

Stefan J. Turneaure¹ and Pinaki Das²

¹*Institute for Shock Physics, Washington State University, Pullman, Washington 99164, USA*

²*Dynamic Compression Sector, Institute for Shock Physics, Washington State University, Argonne, Illinois 60439, USA*



(Received 31 January 2022; revised 18 April 2022; accepted 25 April 2022; published 9 May 2022)

Single-pulse (~ 100 -ps duration) extended x-ray absorption fine structure (EXAFS) measurements were obtained in laser-shocked Pt to examine atomic vibrational properties and to determine temperatures for shock pressures from 72 to 325 GPa. Pt x-ray absorption spectra were recorded while a planar shock wave was propagating through the Pt sample. The absorption spectrum corresponding to the shocked Pt was obtained by subtracting the ambient Pt contribution from the measured absorption spectrum. Fits to the shocked-state EXAFS data provided Pt lattice parameters consistent with the known Pt Hugoniot and the mean-squared relative displacements (MSRDs) for nearest-neighbor Pt atoms. Pt temperatures in the shocked state, estimated from the MSRDs using the correlated Debye model and correlated Einstein models, were consistent with both the Hugoniot temperatures calculated by integration along the Hugoniot and with the Hugoniot temperatures from published first-principles calculations. However, the agreement between the Hugoniot temperatures from EXAFS measurements and the calculated Hugoniot temperatures is not as good above 200 GPa, likely due to anharmonic effects. The present results demonstrate that single-pulse synchrotron EXAFS measurements in laser-shocked solids are useful for quantitative temperature determination and for examination of vibrational properties, including anharmonicity, at extreme pressure-temperature conditions.

DOI: [10.1103/PhysRevB.105.174103](https://doi.org/10.1103/PhysRevB.105.174103)

I. INTRODUCTION

Shock compression of solids to megabar pressures results in extreme pressure-temperature conditions, where material behind the shock wave has undergone near-discontinuous changes in pressure, density, internal energy, and temperature. Although pressure, density, and internal energy of shocked solids are readily measured using continuum methods and the Rankine-Hugoniot jump conditions [1,2], temperature is significantly more challenging to measure [3]. Optical pyrometry measurements are often used for experimental temperature estimation of shocked solids [3,4]. Such measurements are performed at surfaces in opaque materials such as metals, and significant approximations and modeling are required to determine the temperature of the shock-compressed material [3,4]. Hard x-ray probes for temperature determination are attractive because hard x rays can penetrate through the bulk of shocked metals, overcoming the limitations of surface measurements. In particular, the integrated intensities of x-ray diffraction (XRD) peaks are sensitive to temperature through the XRD Debye-Waller factor [5]. Recently, the relative intensities of several *hkl* XRD peaks in laser-shocked Au and Pt were analyzed in an attempt to determine temperatures in the shocked state [6]. However, in that work, shock temperatures could not be determined because the relative *hkl* XRD peak intensities deviated significantly from their expected relationship based on the XRD Debye-Waller factor; this finding was attributed to shock-wave induced microstructural changes [6].

Extended x-ray absorption fine structure (EXAFS) is an alternative x-ray diagnostic that is sensitive to temperature. In EXAFS, electrons ejected from core atomic states during x-ray absorption scatter from neighboring atoms causing the x-ray absorption amplitude to oscillate with energy above the absorption edge due to either constructive or destructive interference [7,8]. EXAFS provides local structural information around the absorbing atom such as the neighboring atomic species, coordination numbers, and bond lengths. More generally, EXAFS is sensitive to the one-dimensional distribution of interatomic distances for each coordination shell of atomic neighbors [7–9]. Even for a perfect crystal, this distribution function is not a delta function due to zero point motion at $T = 0$ K and due to thermal vibrations at higher temperatures. The effect of the finite distribution of interatomic distances is a reduction in the EXAFS amplitude with photoelectron wave vector k via the EXAFS Debye-Waller factor equal to $e^{-2k^2\sigma^2}$ in the harmonic approximation; σ^2 is the mean-squared relative displacement (MSRD) between a pair of atoms [7–11]. EXAFS measurements as a function of temperature have been utilized extensively at ambient pressure, and have provided insight into vibrational properties including anharmonic effects such as thermal expansion [12] and effective anharmonic pair potential parameters [13–16]. Phenomenological models such as the correlated Debye model [10,11] and the correlated Einstein model [11] have been successfully used to quantitatively model the relation between MSRD (from EXAFS) and temperature [14,17–21].

Sharp XRD peaks are a consequence of long-range order in crystalline materials, and XRD intensities for single-crystal or textured polycrystalline materials are highly sensitive to the orientation of the sample relative to the incident x-ray wave-vector direction. In contrast, EXAFS is sensitive to local structure rather than long-range order, and EXAFS amplitudes are significantly less sensitive to texture in polycrystalline materials. Therefore, temperature determination from EXAFS measurements is expected to be less sensitive to microstructure than temperature determination from XRD measurements [6].

Due to the short duration (nanoseconds) of the dynamically compressed state in laser-shock experiments, EXAFS measurements in dynamically compressed solids are challenging and only a small number of such studies have been published over the past two decades [22–26]. In these studies, structural changes were observed in Ti [22] and Fe [23–25] and compression and temperature were reported for Ti, V, and Fe.

The present paper is focused on *in situ* EXAFS measurements in laser-shocked Pt to examine vibrational properties and temperatures at extreme pressure-temperature conditions. Pt has been examined extensively under both static compression [16,27,28] and dynamic compression [1,29–32], due in part to its role as a pressure standard for static pressure experiments [30,32–36]. Continuum shock-wave measurements have provided pressure and volume in Hugoniot states to over 600 GPa [1,29,30]. Recent *in situ* XRD measurements in laser-shocked Pt showed that the face-centered-cubic (fcc) structure remains the stable solid phase on the Hugoniot to at least 380 GPa [31].

Temperatures of shocked Pt have been calculated by numerical integration along the Hugoniot [1] and from first-principles calculations [37,38]. For temperatures achieved during shock compression above 100 GPa, calculations indicate that electronic thermal excitations make an important contribution to the total heat capacity and Grüneisen parameter [30,37,39]. We have calculated a reference Pt Hugoniot temperature by numerical integration along the Hugoniot incorporating both phonon thermal excitations [34] and electron thermal excitations [39] (see Supplemental Material (SM) [40]). As shown in the SM [40], the independent Pt Hugoniot temperature calculations [37,38] match our reference Pt Hugoniot temperature curve [40]. However, direct measurements of Pt Hugoniot temperatures have not been reported to date and represent an important need for comparing shock and static compression results.

Previous EXAFS measurements for compressed Pt have been limited to static compression up to modest pressures (6 GPa) and temperatures (800 K) [16]. Here, we present L_3 -edge EXAFS measurements in shock-compressed Pt up to 325 GPa (corresponding to $T \sim 7200$ K [37,38,40]) using the recently developed single-pulse synchrotron EXAFS capability located at the Dynamic Compression Sector (DCS) at the Advanced Photon Source [42]. Examination of L -edge EXAFS as opposed to K -edge [22–26] provides the opportunity to examine EXAFS in high atomic number elements such as Pt at relatively low x-ray energies (Pt L_3 edge ~ 11.56 keV).

The paper is organized as follows. Experimental methods for shock pressure determination and x-ray absorption spectroscopy measurements are described in Sec. II. In Sec. III,

we present results and describe the analysis of the shocked Pt EXAFS data within the harmonic approximation to obtain the shocked Pt lattice parameter and the mean-squared relative displacement for nearest-neighbor Pt atoms. In Sec. IV, we provide estimates for shocked Pt temperature using phenomenological models and the MSRD values for shocked Pt from the EXAFS measurements and harmonic approximation analysis. Effects of anharmonicity on the EXAFS analysis are considered in Sec. V. Concluding remarks are provided in Sec. VI.

II. EXPERIMENTAL METHODS

Figure 1(a) shows the configuration used for laser-shocked Pt EXAFS experiments. The experiments were performed in the laser-shock station of the DCS [44]. Details regarding the laser-shock EXAFS capability at the DCS are described in Ref. [42]. The targets consist of an aluminized 50- μm -thick Kapton ablator (Goodfellow) epoxy bonded to a 99.95%-purity Pt foil sample (Goodfellow) with thickness $d_{0,\text{Pt}} = 4.7(1) \mu\text{m}$. The “as-rolled” temper and purity of the Pt is the same as used in the previous *in situ* XRD measurements in laser-shocked Pt [6,31]. A 500- μm -diameter laser drive pulse is focused on the Kapton ablator forming a planar shock wave in the Kapton which then propagates into the Pt foil sample. Pt shock pressures were adjusted by using beam splitters to reduce the energy on target from the 100-J laser and/or by changing the laser drive duration (either 5 or 10 ns).

Velocity interferometry measurements (VISAR [45]) were used to record the velocity history u_{fs} of the Pt free surface. These measurements were used to determine shock pressure $P = \rho_{0,\text{Pt}} U_{sh} u_p$ using the Pt Hugoniot [30] defined by $\rho_{0,\text{Pt}} = 21.45 \text{ g/cc}$ and the following shock-velocity–particle-velocity relation:

$$U_{sh} = 3.641 + 1.541 * u_p. \quad (1)$$

In Eq. (1), u_p (units of km/s) is the particle velocity behind the shock wave and U_{sh} (units of km/s) is the Pt shock-wave velocity. The particle velocity in the Hugoniot state u_p is determined from the measured free-surface velocity u_{fs} by subtracting the calculated particle-velocity increase u_r during isentropic stress release from u_{fs} using the method described in Ref. [1].

$$u_p = u_{fs} - u_r. \quad (2)$$

Eleven experiments were performed at five nominal shock pressures from 72 to 325 GPa, with two or three experiments performed at each nominal pressure to establish reproducibility. The measured Pt free-surface velocity histories show good agreement between experiments at the same nominal pressure [see Fig. 1(b)]. The VISAR shock breakout signal at the rear free surface of the Pt foil is time correlated to the x-ray pulse on the target providing nominal timing in each experiment for when the x-ray pulse passed through the sample relative to the shock-wave propagation [44]. For all experiments, the x-ray absorption measurement occurred while the shock wave was propagating through the Pt, but before the shock wave had reached the Pt free surface.

Broadband x rays originating from a 2.7-cm period undulator are used for the transmission x-ray absorption

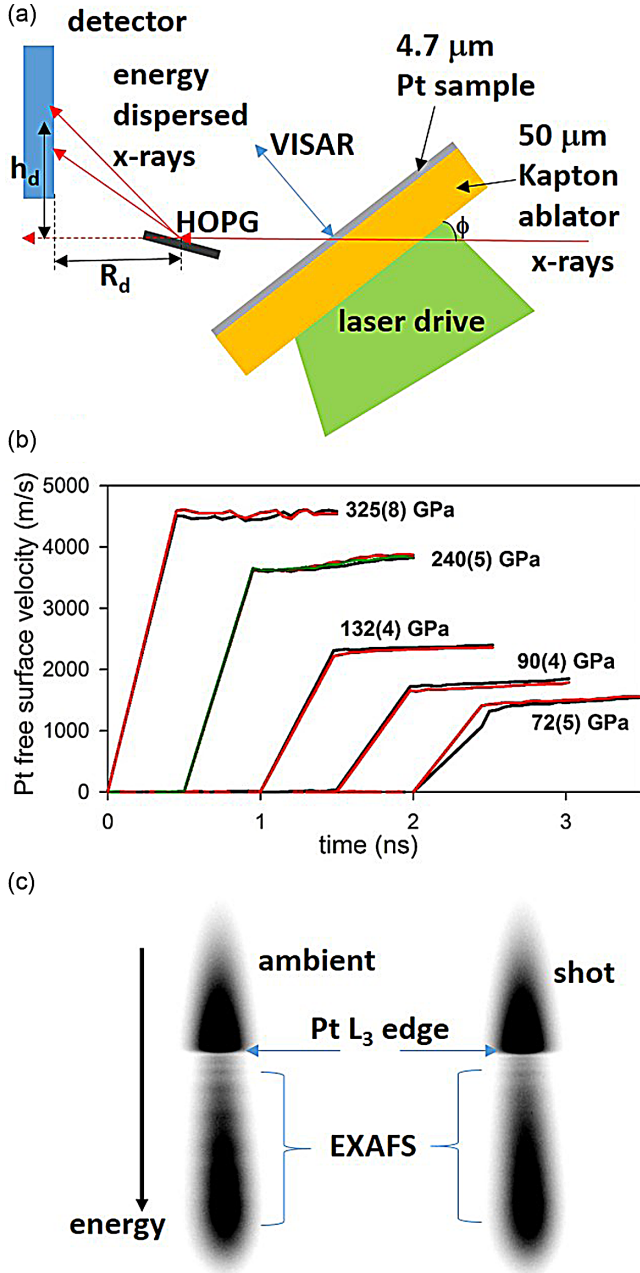


FIG. 1. (a) Configuration for single-pulse EXAFS measurements in laser-shocked Pt (not to scale). (b) Pt free-surface velocity histories for all 11 experiments. Three profiles are shown for 240-GPa shock pressure and two profiles for each of the other four nominal pressures. (c) Representative raw single-pulse x-ray absorption spectra detector images for an ambient Pt target and for a Pt target while a 132-GPa shock wave is propagating through the sample.

measurement. The undulator magnet gap was set to produce a first-harmonic x-ray energy spectrum encompassing the Pt L_3 absorption edge (~ 11.56 keV). Silicon Kirkpatrick-Baez mirrors were used to focus the x-ray beam horizontally and vertically, and to act as a low-pass filter removing higher x-ray harmonics. The x-ray beam at the sample was ~ 50 μm horizontally and ~ 30 μm vertically and was centered on the 500- μm -diameter laser drive spot. A single x-ray pulse (super

bunch in the APS hybrid operation mode) of ~ 100 -ps duration was isolated using an x-ray shutter and two phase-locked x-ray choppers in series [44]. This x-ray pulse passes through the target as shown in Fig. 1(a) before being angularly dispersed by diffraction from a mosaic slab of highly oriented pyrolytic graphite (HOPG) resulting in an angle/x-ray energy correlation. The angularly dispersed x rays are recorded on a flat phosphor-coupled, charge-coupled device (CCD) detector oriented in the vertical plane. The CCD detector has 2048×2048 pixels with 79- μm pitch and the detector plane was located $R_d \sim 2460$ mm downstream from the HOPG/x-ray beam intersection with the central pixel row of the detector $h_d \sim 808$ mm above the direct x-ray beam. The values of R_d and h_d were physically measured to ~ 1 -mm resolution. R_d and h_d were then refined by measuring the detector pixel row number of a Ge K edge, a Pt L_3 edge, and a Au L_3 edge with fixed detector position; precise values for R_d and h_d were determined from the pair of values that provided the best match between measured and calculated pixel row number for the three measured absorption edges.

Figure 1(c) shows representative single-pulse x-ray absorption detector images for an ambient Pt target and for the same Pt target during a 132-GPa shock-wave experiment. Five such ambient spectra were recorded and averaged before each experiment. Five monitor spectra with a target consisting of only a 50- μm -thick Kapton ablator were also recorded both before and after each shock-wave experiment to measure the incident x-ray spectrum without the Pt sample.

III. RESULTS AND ANALYSIS

The raw sample and monitor detector images were integrated horizontally with vertical pixel numbers converted to x-ray energy (E) resulting in curves $I_{\text{sample}}(E)$ corresponding to the intensity transmitted through the sample and $I_{\text{monitor}}(E)$ corresponding to the incident intensity [42]. The absorption spectrum μx , where μ is the x-ray absorption coefficient (units of inverse length) and x is the thicknesses of material through which the x rays pass, is calculated using Eq. (3):

$$\mu x = \ln \left[\frac{I_{\text{monitor}}(E)}{I_{\text{sample}}(E)} \right]. \quad (3)$$

Figure 2(a) shows representative absorption spectra measured for ambient Pt and for Pt during a 132-GPa shock-wave experiment.

Because each shock-wave experiment was timed such that the x-ray absorption measurement occurred after the shock wave had entered the Pt, but before the shock wave had reached the Pt free surface, the total absorption spectrum $(\mu x)_{\text{shot}}$ recorded during each shock-wave experiment is the sum of an ambient sample portion and a shocked sample portion:

$$(\mu x)_{\text{shot}} = f(\mu x)_{\text{ambient}} + (\mu x)_{\text{shocked}}. \quad (4)$$

In Eq. (4), $(\mu x)_{\text{ambient}}$ is the measured absorption spectrum for the fully ambient sample, f is the fraction of the Pt thickness not yet shocked during the x-ray absorption measurement, and $(\mu x)_{\text{shocked}}$ is the absorption spectrum corresponding to the shocked portion of the sample. Although the fraction of the Pt thickness that is unshocked during the

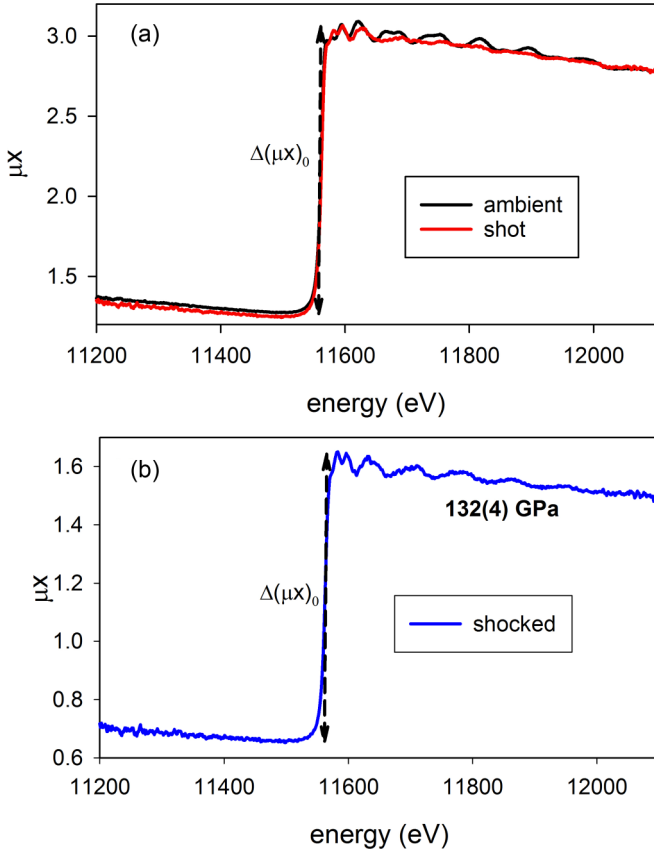


FIG. 2. (a) Representative x-ray absorption spectra for an ambient Pt target and for a Pt target while a 132-GPa shock wave is propagating through the sample (shot). Spectra were obtained from raw data shown in Fig. 1(c). (b) Representative absorption spectrum corresponding to the 132-GPa shock-compressed portion of the Pt sample. The shocked Pt absorption spectrum was obtained by subtracting $f = 46.4\%$ of the ambient absorption spectrum from the shot absorption spectrum.

x-ray absorption measurement is nominally known from the VISAR/x-ray time correlation, the reported uncertainty in this timing is 150 ps [44], which is a substantial fraction of the Pt shock transit time equal to $4.7 \mu\text{m}/U_{\text{sh}}$. Pt shock transit times range from ~ 673 ps at 325 GPa to ~ 948 ps at 72 GPa. Therefore, the parameter f was refined by fitting multiple trial EXAFS spectra determined from trial $(\mu x)_{\text{shot}}$ absorption spectra with varying f values as described in the SM [40]. Figure 2(b) shows a representative $(\mu x)_{\text{shocked}}$ spectrum calculated from the absorption spectra in Fig. 2(a) using Eq. (4) after refining the value of f .

The ATHENA software package [43] was used to convert the absorption spectra μx to the EXAFS $\chi(E)$:

$$\chi(E) = \frac{(\mu x) - (\mu x)_0}{\Delta(\mu x)_0}. \quad (5)$$

In Eq. (5), (μx) is the measured absorption spectrum corresponding to either ambient Pt $(\mu x)_{\text{ambient}}$ or the shocked portion of the Pt $(\mu x)_{\text{shocked}}$. $(\mu x)_0$ is the background absorption spectrum, and $\Delta(\mu x)_0$ is the edge step shown in Fig. 2. The background $(\mu x)_0$ was determined using the AUTOBK routine [46] as implemented in ATHENA [43]. The EXAFS

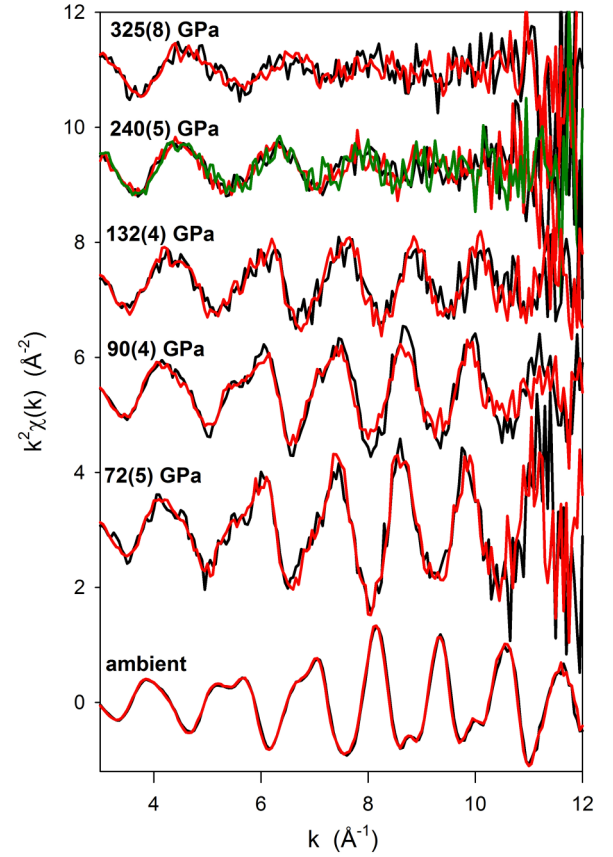


FIG. 3. Pt k^2 -weighted EXAFS. Overlapping ambient Pt EXAFS are averages from two experimental campaigns. Shocked-state Pt EXAFS were calculated using ATHENA [43] after subtracting the appropriate fraction f of $(\mu x)_{\text{ambient}}$ from $(\mu x)_{\text{shot}}$ for each of the 11 experiments. Results from three experiments are shown for 240-GPa pressure and results from two experiments are shown for each of the other four shock pressures. EXAFS at different pressures are offset vertically for visual clarity.

spectra are typically expressed in terms of the photoelectron wave number k :

$$k = \sqrt{\frac{2m_e}{\hbar^2}(E - E_0)}. \quad (6)$$

In Eq. (6), m_e is the electron mass and \hbar is the reduced Planck constant. A value of $E_0 = 11\,565$ eV was used for the Pt L_3 absorption edge energy when determining $\chi(k)$ from μx .

Figure 3 shows the average $k^2\chi(k)$ for ambient Pt along with the $k^2\chi(k)$ corresponding to the shocked Pt for each experiment. The two overlapping average EXAFS curves for ambient Pt correspond to ambient EXAFS averages from experiments performed in two separate campaigns with different x-ray beam/sample angles; ϕ in Fig. 1(a) was either 52° or 38° in the two campaigns. The good match between ambient Pt EXAFS measured with different sample orientations relative to the incident x rays (see Figs. 3 and S2 [40]) demonstrates that the measured Pt EXAFS is insensitive to sample texture, in contrast to previous *in situ* XRD measurements in laser-shocked Pt [6].

Figure 3 also shows good reproducibility between EXAFS from different experiments at the same nominal pressure. The

same EXAFS peaks are observed at all pressures indicating the absence of a structural change, but the peaks shift towards higher k with pressure due to a reduction in the Pt-Pt bond lengths with compression. The EXAFS oscillation amplitudes initially increase relative to the ambient EXAFS oscillation amplitudes at 72 GPa before decreasing at higher shock pressures due to damping of the EXAFS via the EXAFS Debye-Waller factor.

Theoretical EXAFS were fit to the measured Pt EXAFS using the standard EXAFS equation for polycrystalline materials in the harmonic approximation [8]:

$$\chi(k) = S_0^2 \sum_i N_i \frac{f_i(k)}{k R_i^2} \sin[2kR_i + \delta_i(k)] e^{-2R_i/\lambda(k)} e^{-2k^2\sigma_i^2}. \quad (7)$$

Although rigorously the L -edge EXAFS equation has additional complexity, Eq. (7) is still a good approximation for L -edge EXAFS in polycrystalline materials [7] and Pt foil L_3 -edge. T -dependent EXAFS have been successfully fit using the standard EXAFS equation [18]. The sum in Eq. (7) is over scattering paths and the two single scattering paths from the first two coordination shells (paths 1 and 2, respectively) were used for the calculated theoretical EXAFS that was fit to the data. The EXAFS is dominated by path 1, but path 2 was included for completeness. The Pt EXAFS were fit using IFEFFIT as implemented in the ARTEMIS software package [43] with theoretical EXAFS calculated using FEFF6 [47]. Scattering amplitudes $f_i(k)$, phase shifts $\delta_i(k)$ and photoelectron mean-free paths $\lambda(k)$ appearing in the EXAFS equation are calculated in FEFF6 [47]. The number of equivalent paths N_i for each path type are fixed at known values for the fcc structure: 12 for single scattering from nearest neighbors and 6 for single scattering from second-nearest neighbors. The path lengths $2R_i$ are calculable from a single Pt lattice parameter a along with the assumption of a cubic unit cell for the shocked Pt. The mean-squared relative displacements (MSRDs) of each half-path length ($\sigma_i^2 = \langle (r - R_i)^2 \rangle$) act to reduce the EXAFS amplitude as k increases through the EXAFS Debye-Waller factor $e^{-2k^2\sigma_i^2}$, and are free-fitting parameters. S_0^2 is the amplitude reduction factor and ΔE_0 is an energy shift, which accounts for misalignment in edge energies used in calculating k for measured and theoretical $\chi(k)$.

EXAFS fits were performed in R space rather than k space. $\chi(R)$ is obtained by performing the same Fourier transform on both the measured and theoretical $k^n \chi(k)$ where k weights of $n = 1, 2$, and 3 were used. Fitting to $\chi(R)$ rather than $\chi(k)$ filters out the longer path lengths that contribute high-frequency oscillations to $\chi(k)$. To encompass the first two paths while excluding the $\chi(R)$ contributions from longer scattering paths not included in the theoretical calculation, fits to the ambient and shocked Pt $\chi(R)$ were performed for $R = 1.2\text{--}3.62 \text{ \AA}$ and $R = 1.2\text{--}3.4 \text{ \AA}$, respectively. All fits to our ambient and shocked Pt EXAFS are performed using minimum values of the photoelectron wave number k_{\min} from 3.5 to 4.5 \AA^{-1} in the Fourier transforms because of energy-resolution limitations at lower k (see Fig. S2(b)) [40]. For fits to the shocked Pt data, the amplitude reduction factor and energy shift were fixed at values obtained from fits to the ambient Pt EXAFS: $S_0^2 = 0.74(0.04)$ and $\Delta E_0 = 7.8(0.9) \text{ eV}$ [40]. Thus, for shocked Pt

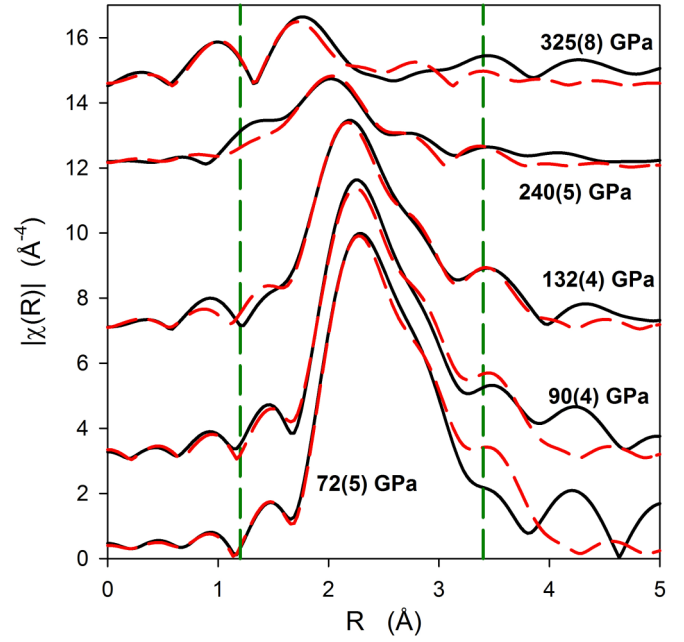


FIG. 4. Representative results and fits to the Fourier transform of the k^3 -weighted EXAFS at each nominal pressure. Fourier transforms are from $k = 4$ to 10 \AA^{-1} . Black lines are from the data and red dashed lines are from fits to the data from $R = 1.2$ to 3.4 \AA (vertical green dashed lines). EXAFS at different pressures are offset vertically for visual clarity.

EXAFS, the remaining free-fitting parameters are the Pt lattice parameter a and the MSRDs.

Representative fits to the measured Fourier-transformed k^3 -weighted EXAFS for shocked Pt are shown in Fig. 4 for each nominal pressure. A systematic shift to lower R with increasing shock pressure is apparent, indicating a decrease in nearest-neighbor bond lengths with shock pressure. Additionally, the peak amplitude of $|\chi(R)|$ decreases with increasing shock pressure due to a reduction in the $\chi(k)$ amplitudes with shock pressure due to the EXAFS Debye-Waller factor. Values of a and σ_1^2 obtained from EXAFS fits for each experiment are shown vs shock pressure in Figs. 5 and 6, respectively. Uncertainties in a and σ_1^2 were obtained by performing multiple EXAFS fits as described in the SM [40].

The Pt lattice parameters a obtained from the EXAFS fits are compared with the lattice parameters calculated from the Pt Hugoniot assuming isotropic lattice compression in Fig. 5:

$$a_{\text{Hugoniot}} = a_0 [1 - u_p / U_{\text{sh}}]^{1/3}. \quad (8)$$

Here, a_0 is the ambient Pt lattice parameter and a_{Hugoniot} is the Pt lattice parameter in the Hugoniot state. The continuum Pt Hugoniot is accurately known [30] and the lattice parameters from the continuum Hugoniot assuming isotropic lattice compression match the lattice parameters of laser-shocked Pt from *in situ* XRD measurements [31]. Therefore, the Pt lattice parameters from the continuum Hugoniot serve as a benchmark for determining the accuracy of the present EXAFS measurements and fitting results. Within uncertainty, the Pt lattice parameters obtained from EXAFS fitting in the harmonic approximation are consistent with the continuum Hugoniot results over the entire pressure range. However, we

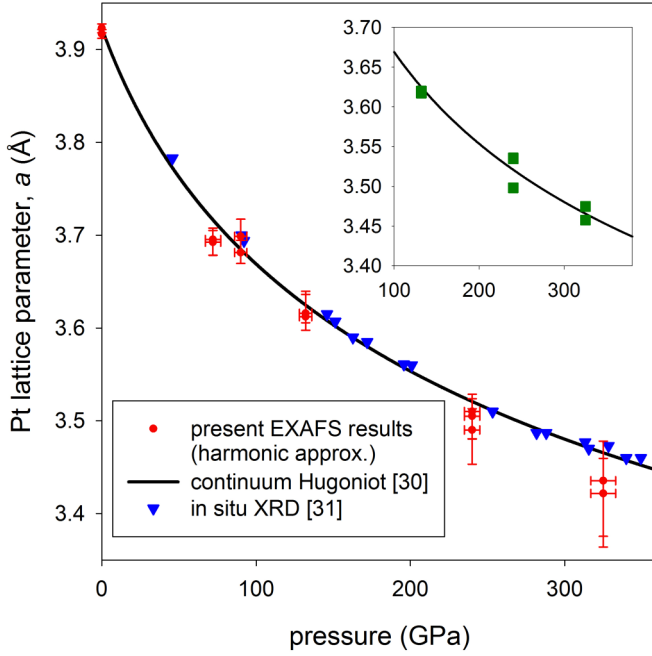


FIG. 5. Pt lattice parameter vs shock pressure. Red circles are lattice parameters for shocked Pt obtained from fits to the shocked Pt EXAFS using the harmonic approximation. The black solid line is from the continuum Pt Hugoniot [30] assuming isotropic lattice compression (cubic unit cell). Blue triangles are shocked Pt lattice parameters from *in situ* XRD measurements [31]. The inset shows that above 200 GPa Pt lattice parameters (green squares), obtained from EXAFS fits incorporating anharmonic effects via the third cumulant $\sigma^{(3)}$, match expected values (black line) better than the Pt lattice parameters obtained from EXAFS fits using the harmonic approximation (red circles in main figure).

note that the Pt lattice parameters from EXAFS are systematically less than the Pt lattice parameters from the continuum Hugoniot above 200 GPa. This deviation at large shock pressures is due to anharmonicity, discussed further in Sec. V.

The MSRD values σ_1^2 for nearest-neighbor Pt atoms are plotted vs shock pressure in Fig. 6 and provide information on vibrational amplitudes for Pt under extreme pressure-temperature conditions. At 72 GPa, σ_1^2 is comparable to the ambient σ_1^2 value, but for higher shock pressures σ_1^2 increases roughly linearly with shock pressure. For comparison with the experimentally determined σ_1^2 values, we plot calculated σ_1^2 curves for 296 K isothermal compression (dashed line). The room-temperature isothermal σ_1^2 values were calculated using the correlated Debye (CD) model [10,11].

$$\sigma_1^2 = \frac{3\hbar^2}{Mk_B\theta_D} \int_0^1 dx x \coth\left(\frac{x\theta_D}{2T}\right) \left[1 - \frac{\sin(xR_1k_D)}{xR_1k_D}\right]. \quad (9)$$

Here, $k_D = (6\pi^2/V_p)^{1/3}$, where $V_p = a^3/4$ is the volume of the primitive Pt unit cell, M is the mass of a Pt atom, and k_B is the Boltzmann constant. In the CD model, σ_1^2 is calculable from the lattice parameter a , the average path length for nearest-neighbor Pt atoms $2R_1$, which depends only on a , the Debye temperature θ_D , and the temperature T . The Debye temperature θ_D increases with volume compression and is calculated using the Pt volume-dependent Grüneisen

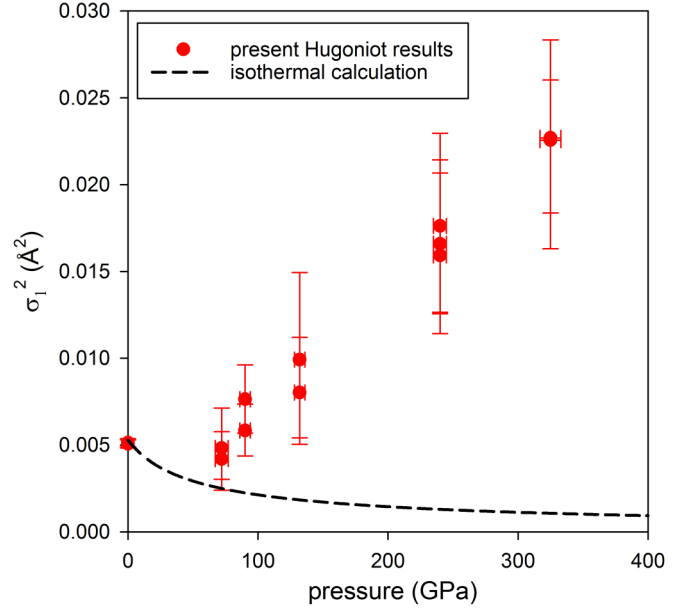


FIG. 6. Mean-squared relative displacement σ_1^2 for Pt nearest neighbors. Red symbols are Hugoniot results from fits to the shocked Pt EXAFS data. The black dashed line is the calculated σ_1^2 curve for isothermal (296 K) compression using the correlated Debye model with volume-dependent Debye temperatures calculated using the Pt Grüneisen parameter $\Gamma_{ph}(V)$ given in Ref. [34].

parameter due to phonon excitations $\Gamma_{ph}(V)$ from Ref. [34] with $\theta_{D0} = 230$ K [30,34].

$$\theta_D = \theta_{D0} e^{-\int_{V_0}^V \frac{\Gamma_{ph}(V')}{V'} dV'}. \quad (10)$$

Figure 6 shows that isothermal compression results in a significant reduction of σ_1^2 with pressure. Such a reduction in σ_1^2 with compression was previously reported for statically compressed Pt to 6 GPa [16] and in theoretical calculations for Pt to 14 GPa [20], and is due to a reduction in the atomic vibrational amplitude as material stiffness increases with compression. The observed large increase in σ_1^2 with shock pressure indicates that the high temperatures achieved during shock compression of Pt beyond 72 GPa outweigh the effects of increasing material stiffness on atomic vibrational amplitudes. Temperature determination from the measured σ_1^2 values is discussed next.

IV. TEMPERATURE DETERMINATION

To obtain temperatures from measured MSRDs, a model relating temperature to MSRD is required. Ideally, the temperature dependence of the MSRD would be calculated from the actual projected vibrational density of states $\rho_R(\omega)$ [48], but in practice it is more convenient to use phenomenological models such as the CD model [10,11] [see Eq. (9)] or the correlated Einstein (CE) model [11]. Such models have been used successfully to match the temperature dependence of the MSRD at ambient pressure in a variety of fcc metals [13,14,17–19,49,50]. For nearest-neighbor scattering in fcc metals, the Einstein temperature θ_E is approximately equal to 3/4 the Debye temperature θ_D in the CD model [9,11]; this is

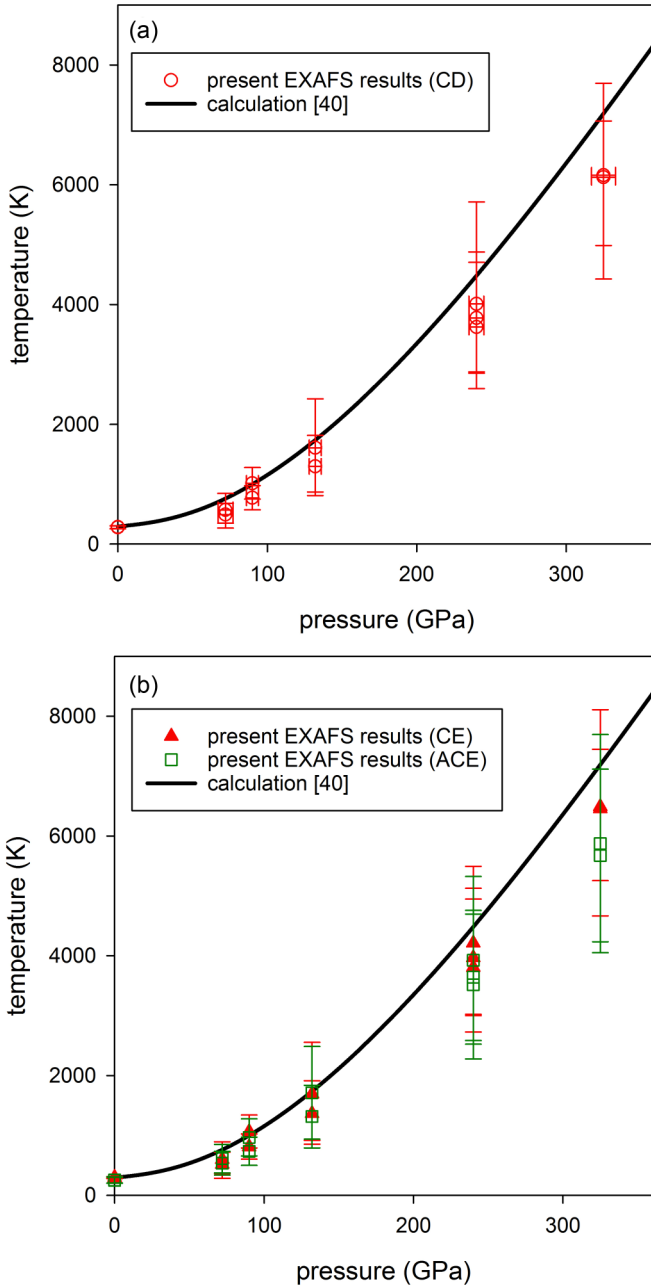


FIG. 7. Temperature of shock-compressed Pt. The black solid lines are the reference Pt Hugoniot temperature curves calculated by numerical integration along the Hugoniot [40]. (a) Red circles are shocked Pt temperatures from EXAFS calculated from the σ_1^2 values shown in Fig. 6 using the CD model. (b) Red triangles are shocked Pt temperatures from EXAFS calculated from the σ_1^2 values shown in Fig. 6 using the CE model with volume-dependent Einstein temperatures θ_E equal to $3/4\theta_D$ [9,11]. Green squares are temperatures for shocked Pt from EXAFS using the ACE as described in the text.

confirmed for Pt at ambient pressure where fits to T-dependent Pt EXAFS using the CE model resulted in $\theta_E = 174$ K [19].

Figures 7(a) and 7(b) show the Pt Hugoniot temperatures determined from the measured MSRDs using CD and CE models, respectively. For the CD model, the volume-dependent Debye temperature θ_D is calculated using Eq. (10) with $\Gamma_{ph}(V)$ from Ref. [34]. The temperatures using the

CE model are about 5% larger than when using the CD model, a difference smaller than the temperature uncertainties introduced from the EXAFS fitting uncertainties in σ_1^2 . For the three lowest shock pressures examined (below 150 GPa), the temperatures determined from EXAFS using the CD and CE models are in good agreement with the calculated reference Pt Hugoniot temperature (black curves in Fig. 7) determined by integration along the Hugoniot as described in the SM [40]. At shock pressures above 200 GPa, the temperatures determined from EXAFS, although in agreement with the calculated reference Pt Hugoniot temperatures [40] within uncertainty, lie systematically below the calculated reference Pt Hugoniot temperatures [40]. This deviation is likely due to anharmonic effects as discussed below.

V. ANHARMONIC EFFECTS

An additional factor we now consider in our EXAFS analysis and temperature determination is the effect of lattice anharmonicity. For a given pressure, anharmonic effects become more important with increased temperature as atomic vibrational amplitudes become larger. A convenient formalism used to examine the effects of anharmonicity on EXAFS is the use of an effective potential for the relative displacement between two atoms [12,49–51]:

$$V_{\text{eff}}(r) = \frac{1}{2}k_{\text{eff}}r^2 + k_{3\text{eff}}r^3 + k_{4\text{eff}}r^4 + \dots \quad (11)$$

Here, r is the difference in the instantaneous bond length from the average bond length. The harmonic approximation corresponds to $k_{3\text{eff}}$ and $k_{4\text{eff}}$ and higher-order coefficients equal to zero. When anharmonic terms are important, the EXAFS equation has additional terms that can be described by the cumulant expansion method [8,9,51,52]. The second cumulant is the MSRD σ^2 already discussed in the harmonic approximation analysis. The third cumulant $\sigma^{(3)}$ and fourth cumulant $\sigma^{(4)}$ are defined by $\sigma^{(3)} = \langle (r-R)^3 \rangle$ and $\sigma^{(4)} = \langle (r-R)^4 \rangle - 3(\sigma^2)^2$, respectively, where R is the mean distance between atoms. These higher cumulants represent deviations from a Gaussian distribution for interatomic separations. The third cumulant appears as an additional phase shift in the sine term in Eq. (7) [8] and $\sigma^{(3)}$ is therefore highly correlated with the lattice parameter a through the path length $2R$ when fitting. The fourth cumulant primarily affects the EXAFS amplitude through the EXAFS Debye-Waller factor, which becomes $e^{-[2k^2\sigma^2 - \frac{2}{3}k^4\sigma^{(4)}]}$ [8]. The second and fourth cumulants are highly correlated during EXAFS fitting as they both affect EXAFS amplitudes with increasing photoelectron wave vector k .

With the exception of Ref. [24], which incorporated the third cumulant, previous analyses of EXAFS in dynamically compressed solids have not included anharmonic effects. We follow the approach of Ref. [24] and apply the anharmonic correlated Einstein (ACE) model where the $k_{3\text{eff}}r^3$ term in Eq. (11) is treated as a perturbation and higher-order anharmonic potential terms are neglected. The Einstein temperature θ_E is related to the potential in Eq. (11) via $\theta_E = \frac{\hbar}{k_B} \sqrt{\frac{2k_{\text{eff}}}{M}}$. In the high-temperature limit (above θ_D) and using perturbation theory, the MSRD σ_1^2 contains a contribution from the third

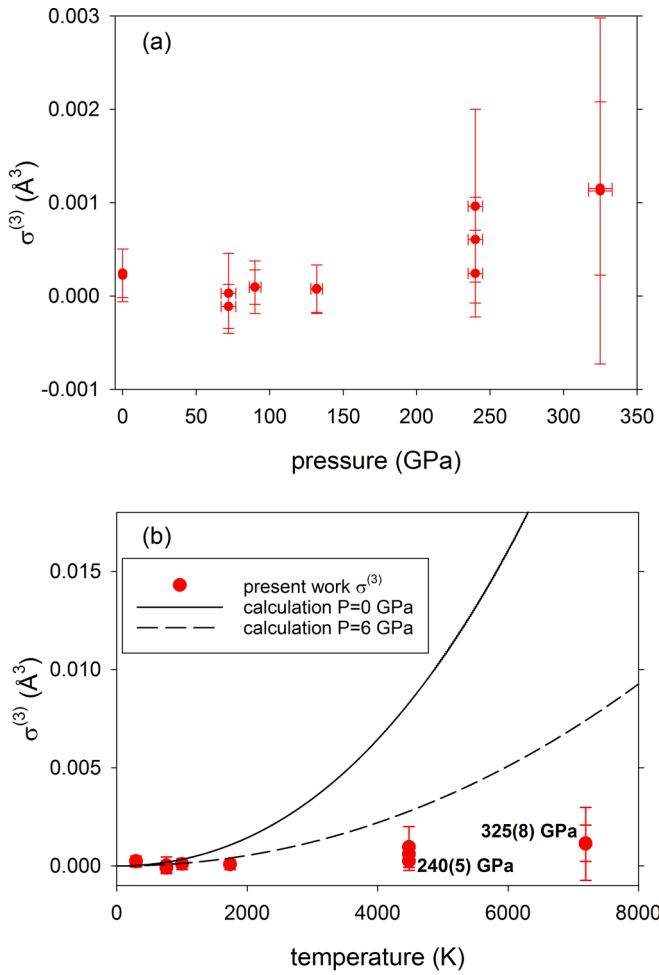


FIG. 8. (a) Third cumulant $\sigma^{(3)}$ for shocked Pt from EXAFS fits vs shock pressure. (b) Red symbols are the same $\sigma^{(3)}$ plotted in (a) as a function of shocked Pt temperature [40]. The 0- and 6-GPa isobaric $\sigma^{(3)}$ curves show calculated temperature dependence of $\sigma^{(3)}$ using the effective potential parameters k_{eff} and $k_{3\text{eff}}$ reported in Ref. [16].

cumulant [13,49,50]:

$$\sigma_1^2 \approx \sigma_E^2 + (\sigma^{(3)}/\sigma_E^2)^2. \quad (12)$$

In Eq. (12), $\sigma_E^2 = \frac{2\hbar^2 T}{Mk_B\theta_E^2}$, which corresponds to the harmonic contribution to the MSRD in the CE model in the high- T limit. Additionally, in the high-temperature limit, the temperature dependence of the third cumulant $\sigma^{(3)}$ can also be expressed in terms of k_{eff} and $k_{3\text{eff}}$ [13,50]:

$$\sigma^{(3)} \approx \frac{-6k_{3\text{eff}}(k_B T)^2}{k_{\text{eff}}^3} \left\{ 1 + \frac{144k_{3\text{eff}}^2(k_B T)}{k_{\text{eff}}^3} \right\}. \quad (13)$$

To examine possible anharmonic effects, we fit the shocked Pt EXAFS from each experiment including the third cumulant $\sigma^{(3)}$ as a fitting parameter. Including $\sigma^{(3)}$ in the fits resulted in negligible changes in the MSRD σ_1^2 values compared to the harmonic approximation fit results. Fitting results for $\sigma^{(3)}$ are shown in Fig. 8(a). Below 150 GPa, the third cumulant is near zero within fitting uncertainties, but for the two shock pressures above 200 GPa, $\sigma^{(3)}$ is systematically

larger, suggesting the importance of anharmonic effects above ~ 200 -GPa shock pressure where shock temperatures exceed 3300 K. The importance of anharmonic effects above 200 GPa is also supported by the fact that incorporating $\sigma^{(3)}$ in the fits significantly improves the match between lattice parameters a from EXAFS fits and the known Pt lattice parameters calculated from the continuum Pt Hugoniot [30] (see Fig. 5 inset).

For comparison with our third cumulant results for shocked Pt, we plot isobaric 0 and 6 GPa $\sigma^{(3)}(T)$ curves calculated using Eq. (13) and experimentally determined Pt effective potential parameters k_{eff} and $k_{3\text{eff}}$ from Ref. [16] in Fig. 8(b). The calculations show that even a modest pressure of 6 GPa substantially reduces the third cumulant curve relative to the ambient-pressure third cumulant curve. Our experimental results for $\sigma^{(3)}$ above 200 GPa indicate a further substantial isothermal reduction in $\sigma^{(3)}$ with increasing pressure. This implies that the effective Pt interatomic potential becomes less skewed with increasing compression.

We used Eq. (12) corresponding to the ACE model to calculate the shocked Pt temperature using the σ_1^2 and $\sigma^{(3)}$ values shown in Figs. 6 and 8, respectively. The resulting shocked Pt temperatures are plotted in Fig. 7(b) (green squares). Below 150 GPa, there is negligible change in the calculated temperatures between the CE and ACE models due to the small $\sigma^{(3)}$ values at these pressures. In contrast, above 200 GPa, there is a moderate decrease in the calculated temperature using the ACE model compared to the CE model. Note that the structure of Eq. (12) implies that the temperature determined from the ACE model will always be less than the temperature determined from the CE model when only the third cumulant is incorporated as an anharmonic perturbation. Thus, using the ACE model with only the third cumulant cannot improve the agreement between shocked Pt temperature from EXAFS analysis and our reference calculated Pt Hugoniot temperatures [40].

Ping *et al.* reported that analysis of EXAFS in dynamically compressed Fe required cumulants higher than the third when $T/\theta_D > 8$ [24]. For shocked Pt at 240 and at 325 GPa, T/θ_D is approximately 10 and 15, respectively. Thus, it is likely that the fourth cumulant $\sigma^{(4)}$ becomes important for shocked Pt above 200 GPa. The fourth cumulant $\sigma^{(4)}$ has been measured at ambient pressure for the fcc metals Pt [53], Ag [50], Au [21], Cu [14], and Ni [14] and all reported $\sigma^{(4)}$ values were greater than zero. When the actual distribution of atomic separations has a positive $\sigma^{(4)}$ value, noninclusion of $\sigma^{(4)}$ in the fitting will result in an underestimation of σ^2 given the form of the EXAFS Debye-Waller factor $e^{-[2k^2\sigma^2 - \frac{2}{3}k^4\sigma^{(4)}]}$. An underestimation of σ^2 will translate to an underestimation of temperature. For Au at ambient pressure, noninclusion of $\sigma^{(4)}$ in the EXAFS fitting was indeed found to result in a significant underestimation of σ^2 at elevated temperatures [21]. Thus, noninclusion of $\sigma^{(4)}$ in the EXAFS fitting for Pt shocked above 200 GPa is a likely explanation for the small systematic deviation between shocked Pt temperatures determined from our EXAFS measurements and our reference Pt Hugoniot temperatures from numerical integration along the Hugoniot [40]. The limited k range and noise present in the single-shot EXAFS data in laser-shocked Pt

prevented us from determining reliable $\sigma^{(4)}$ values from the EXAFS fitting to test this hypothesis.

VI. CONCLUDING REMARKS

In summary, we have performed Pt L_3 -edge EXAFS measurements in laser-shocked Pt up to 325 GPa. The shocked Pt EXAFS were examined in the harmonic approximation to determine the lattice parameter and the mean-squared relative displacement σ_1^2 of nearest-neighbor Pt atoms along the Hugoniot. Lattice parameters determined from our EXAFS measurements are in agreement with the continuum Pt Hugoniot [30] and with previous *in situ* XRD measurements [31], but incorporation of anharmonic effects via the third cumulant in the EXAFS fitting significantly improved the agreement above 200 GPa. Temperatures for shocked Pt were estimated from the σ_1^2 values determined from the EXAFS fitting using the correlated Debye model [10,11], the correlated Einstein model [11], and the anharmonic correlated Einstein model as in Ref. [24]. Overall, the resulting shocked Pt temperature estimates from EXAFS are in general agreement with calculated Pt Hugoniot temperatures [37,38,40], but trend systematically lower than the calculated Pt Hugoniot temperatures above 200 GPa. This deviation is likely due to anharmonic effects related to the fourth cumulant $\sigma^{(4)}$. Due to measurement noise and limited k range, we were unable to accurately determine the fourth cumulant $\sigma^{(4)}$ contribution to the EXAFS Debye-Waller factor $e^{-[2k^2\sigma^2 - \frac{2}{3}k^4\sigma^{(4)}]}$ and have therefore neglected $\sigma^{(4)}$ in the EXAFS analysis which likely results in an underestimation of the σ^2 values obtained from EXAFS fitting above 200 GPa shock pressure. This is a fundamental difficulty for other materials as well, because for large shock temperatures where $\sigma^{(4)}$ may become important in the analysis, the EXAFS amplitude decays rapidly with k further limiting the k range available to discriminate between σ^2 and $\sigma^{(4)}$ during the EXAFS fitting process. Therefore, it would be desirable

in future work to extend the measurement k range and to improve the signal-to-noise ratio such that the fourth cumulant can be incorporated in the EXAFS fitting. Alternatively, complementary quantum molecular dynamics simulations such as those reported in Ref. [24] could be performed to determine if cumulants higher than the third need to be included in the EXAFS analysis.

Compared to previous analysis of *in situ* XRD measurements [6] in the same type of laser-shocked Pt material to comparable stresses, the present EXAFS measurements in laser-shocked Pt are significantly less sensitive to microstructure—allowing us to examine Pt vibrational properties and to determine Pt temperature in the shocked state. As a result, EXAFS measurements in laser-shocked solids are expected to be useful for constraining vibrational properties and temperature under extreme conditions in other materials with results serving as a benchmark for future theoretical work.

ACKNOWLEDGMENTS

Kory Green, Ray Gunawidjaja, Yuelin Li, Korey Mercer, Adam Schuman, Nick Sinclair, Austin Spencer, Xiaoming Wang, and Jun Zhang at the Dynamic Compression Sector (Advanced Photon Source, Argonne National Laboratory) are gratefully acknowledged for their assistance with the experiments. Yogendra Gupta and Paulo Rigg are thanked for providing valuable comments on a draft manuscript. This work was supported by the U.S. Department of Energy (DOE) National Nuclear Security Administration (NNSA) under Award No. DE-NA0003957, and experiments were carried out at the Dynamic Compression Sector, managed and operated by Washington State University. This research used resources of the Advanced Photon Source, a DOE Office of Science User Facility operated for the DOE Office of Science by Argonne National Laboratory under Contract No. DE-AC02-06CH11357.

-
- [1] R. G. McQueen, S. P. Marsh, J. W. Taylor, J. M. Fritz, and W. J. Carter, in *High Velocity Impact Phenomena*, edited by R. Kinslow (Academic, New York, 1970), Chap. VII and Appendixes D and E.
 - [2] G. E. Duvall and R. A. Graham, *Rev. Mod. Phys.* **49**, 523 (1977).
 - [3] T. M. Hartsfield, B. M. La Lone, G. D. Stevens, L. R. Veaser, and D. H. Dolan, *J. Appl. Phys.* **128**, 015903 (2020).
 - [4] B. J. Jensen, T. M. Hartsfield, D. B. Holtkamp, F. J. Cherne, R. B. Corrow, T. E. Graves, and A. J. Iverson, *Phys. Rev. B* **102**, 214105 (2020).
 - [5] B. E. Warren, *X-ray Diffraction* (Addison-Wesley, Reading, MA, 1969).
 - [6] S. M. Sharma and Y. M. Gupta, *Phys. Rev. B* **104**, 064113 (2021).
 - [7] P. A. Lee, P. H. Citrin, P. Eisenberger, and B. M. Kincaid, *Rev. Mod. Phys.* **53**, 769 (1981).
 - [8] J. J. Rehr and R. C. Albers, *Rev. Mod. Phys.* **72**, 621 (2000).
 - [9] G. Dalba and P. Fornasini, *J. Synchrotron Radiat.* **4**, 243 (1997).
 - [10] G. Beni and P. M. Platzman, *Phys. Rev. B* **14**, 1514 (1976).
 - [11] E. Sevillano, H. Meuth, and J. J. Rehr, *Phys. Rev. B* **20**, 4908 (1979).
 - [12] A. I. Frenkel and J. J. Rehr, *Phys. Rev. B* **48**, 585 (1993).
 - [13] E. A. Stern, P. Livins, and Z. Zhang, *Phys. Rev. B* **43**, 8850 (1991).
 - [14] I. V. Pirog, T. I. Nedoseikina, I. A. Zarubin, and A. T. Shuvaev, *J. Phys.: Condens. Matter* **14**, 1825 (2002).
 - [15] M. Okube and A. Yoshiasa, *J. Synchrotron Radiat.* **8**, 937 (2001).
 - [16] M. Okube, A. Yoshiasa, O. Ohtaka, and Y. Katayama, *High Pressure Res.* **23**, 247 (2003).
 - [17] W. Bohmer and P. Rabe, *J. Phys. C: Solid State Phys.* **12**, 2465 (1979).
 - [18] E. C. Marques, D. R. Sandstrom, F. W. Lytle, and R. B. Gregor, *J. Chem. Phys.* **77**, 1027 (1982).
 - [19] G. S. Knapp, H. K. Pan, and J. M. Tranquada, *Phys. Rev. B* **32**, 2006 (1985).

- [20] N. B. Duc, V. Q. Tho, T. S. Tien, D. Q. Khoa, and H. K. Hieu, *Radiat. Phys. Chem.* **149**, 61 (2018).
- [21] Q. Ye, Y. Hu, X. Duan, H. Liu, H. Zhang, C. Zhang, L. Sun, W. Yang, W. Xu, Q. Cai, Z. Wang, and S. Jiang, *J. Synchrotron Radiat.* **27**, 436 (2020).
- [22] B. Yaakobi, D. D. Meyerhofer, T. R. Boehly, J. J. Rehr, B. A. Remington, P. G. Allen, S. M. Pollaine, and R. C. Albers, *Phys. Rev. Lett.* **92**, 095504 (2004).
- [23] B. Yaakobi, T. R. Boehly, D. D. Meyerhofer, T. J. B. Collins, B. A. Remington, P. G. Allen, S. M. Pollaine, H. E. Lorenzana, and J. H. Eggert, *Phys. Rev. Lett.* **95**, 075501 (2005).
- [24] Y. Ping, F. Coppari, D. G. Hicks, B. Yaakobi, D. E. Fratanduono, S. Hamel, J. H. Eggert, J. R. Rygg, R. F. Smith, D. C. Swift, D. G. Braun, T. R. Boehly, and G. W. Collins, *Phys. Rev. Lett.* **111**, 065501 (2013).
- [25] R. Torchio, F. Occelli, O. Mathon, A. Sollier, E. Lescoute, L. Videau, T. Vinci, A. Benuzzi-Mounaix, J. Headspith, W. Helsby, S. Bland, D. Eakins, D. Chapman, S. Pascarelli, and P. Loubeyre, *Sci. Rep.* **6**, 26402 (2016).
- [26] B. Yaakobi, T. R. Boehly, T. C. Sangster, D. D. Meyerhofer, B. A. Remington, P. G. Allen, S. M. Pollaine, H. E. Lorenzana, K. T. Lorenz, and J. A. Hawreliak, *Phys. Plasmas* **15**, 062703 (2008).
- [27] A. Dewaele, P. Loubeyre, and M. Mezouar, *Phys. Rev. B* **70**, 094112 (2004).
- [28] S. Anzellini, V. Monteseguro, E. Bandiello, A. Dewaele, L. Burakovsky, and D. Errandonea, *Sci. Rep.* **9**, 13034 (2019).
- [29] J. A. Morgan, *High Temp. - High Pressures* **6**, 195 (1974).
- [30] N. C. Holmes, J. A. Moriarty, G. R. Gathers, and W. J. Nellis, *J. Appl. Phys.* **66**, 2962 (1989).
- [31] S. M. Sharma, S. J. Turneaure, J. M. Winey, and Y. M. Gupta, *Phys. Rev. Lett.* **124**, 235701 (2020).
- [32] D. E. Fratanduono, M. Millot, D. G. Braun, S. J. Ali, A. Fernandez-Panella, C. T. Seagle, J.-P. Davis, J. L. Brown, Y. Akahama, R. G. Kraus, M. C. Marshall, R. F. Smith, E. F. O'Bannon, III, J. M. McNaney, and J. H. Eggert, *Science* **372**, 1063 (2021).
- [33] M. Matsui, E. Ito, T. Katsura, D. Yamazaki, T. Yoshino, A. Yokoyama, and K. Funakoshi, *J. Appl. Phys.* **105**, 013505 (2009).
- [34] M. Yokoo, N. Kawai, K. G. Nakamura, K.-i. Kondo, Y. Tange, and T. Tsuchiya, *Phys. Rev. B* **80**, 104114 (2009).
- [35] Y. Fei, A. Ricolleau, K. Mibe, M. Frank, G. Shen, and V. Prakapenka, *Proc. Natl Acad. Sci.* **104**, 9182 (2007).
- [36] S. Ono, J. P. Brodholt, and G. D. Price, *J. Phys. Chem. Solids* **72**, 169 (2011).
- [37] T. Sun, K. Umemoto, Z. Wu, J.-C. Zheng, and R. M. Wentzcovitch, *Phys. Rev. B* **78**, 024304 (2008).
- [38] V. M. Elkin, V. N. Mikhaylov, A. A. Ovechkin, and N. A. Smirnov, *J. Phys.: Condens. Matter* **32**, 435403 (2020).
- [39] T. Tsuchiya and K. Kawamura, *Phys. Rev. B* **66**, 094115 (2002).
- [40] See Supplemental Material at <http://link.aps.org/supplemental/10.1103/PhysRevB.105.174103> for Pt Hugoniot temperature calculations, ambient Pt EXAFS results and fitting, refinement of the ambient fraction of Pt during EXAFS measurements, and details on how the uncertainties in the Pt lattice parameters and MSRDs were determined, and it includes Refs. [41–44].
- [41] L. Zhang, R. Si, H. Liu, N. Chen, Q. Wang, K. Adai, Z. Wang, J. Chen, Z. Song, J. Li, M. N. Banis, R. Li, T.-K. Sham, M. Gu, L.-M. Liu, G. A. Botton, and X. Sun, *Nat. Commun.* **10**, 4936 (2019).
- [42] P. Das, J. A. Klug, N. Sinclair, X. Wang, Y. Toyoda, Y. Li, B. Williams, A. Schuman, J. Zhang, and S. J. Turneaure, *Rev. Sci. Instrum.* **91**, 085115 (2020).
- [43] B. Ravel and M. Newville, *J. Synchrotron Radiat.* **12**, 537 (2005).
- [44] X. Wang, P. Rigg, J. Sethian, N. Sinclair, N. Weir, B. Williams, J. Zhang, J. Hawreliak, Y. Toyoda, Y. Gupta, Y. Li, D. Broege, J. Bromage, R. Earley, D. Guy, and J. Zuegel, *Rev. Sci. Instrum.* **90**, 053901 (2019).
- [45] L. M. Barker and R. E. Hollenbach, *J. Appl. Phys.* **43**, 4669 (1972).
- [46] M. Newville, P. Livins, Y. Yacoby, J. J. Rehr, and E. A. Stern, *Phys. Rev. B* **47**, 14126 (1993).
- [47] S. I. Zabinsky, J. J. Rehr, A. Ankudinov, R. C. Albers, and M. J. Eller, *Phys. Rev. B* **52**, 2995 (1995).
- [48] F. D. Vila, J. J. Rehr, H. H. Rossner, and H. J. Krappe, *Phys. Rev. B* **76**, 014301 (2007).
- [49] N. Van Hung and J. J. Rehr, *Phys. Rev. B* **56**, 43 (1997).
- [50] J. Haug, A. Chasse, R. Schneider, H. Kruth, and M. Dubiel, *Phys. Rev. B* **77**, 184115 (2008).
- [51] P. Fornasini and R. Grisenti, *J. Synchrotron Radiat.* **22**, 1242 (2015).
- [52] G. Bunker, *Nucl. Instrum. Methods* **207**, 437 (1983).
- [53] Y. Nishihata, J. Mizuki, S. Emura, and T. Uruga, *J. Synchrotron Radiat.* **8**, 294 (2001).